LETTER

doi:10.1038/nature12081

Optical addressing of an individual erbium ion in silicon

Chunming Yin[1], Milos Rancic[2], Gabriele G. de Boo[1], Nikolas Stavrias[3], Jeffrey C. McCallum[3], Matthew J. Sellars[2] & Sven Rogge[1]

The detection of electron spins associated with single defects in solids is a critical operation for a range of quantum information and measurement applications under development[1–9]. So far, it has been accomplished for only two defect centres in crystalline solids: phosphorus dopants in silicon, for which electrical read-out based on a single-electron transistor is used[1], and nitrogen–vacancy centres in diamond, for which optical read-out is used[4–6]. A spin read-out fidelity of about 90 per cent has been demonstrated with both electrical read-out[1] and optical read-out[10,11]; however, the thermal limitations of the former and the poor photon collection efficiency of the latter make it difficult to achieve the higher fidelities required for quantum information applications. Here we demonstrate a hybrid approach in which optical excitation is used to change the charge state (conditional on its spin state) of an erbium defect centre in a silicon-based single-electron transistor, and this change is then detected electrically. The high spectral resolution of the optical frequency-addressing step overcomes the thermal broadening limitation of the previous electrical read-out scheme, and the charge-sensing step avoids the difficulties of efficient photon collection. This approach could lead to new architectures for quantum information processing devices and could drastically increase the range of defect centres that can be exploited. Furthermore, the efficient electrical detection of the optical excitation of single sites in silicon represents a significant step towards developing interconnects between optical-based quantum computing and silicon technologies.

The potential for hybrid optical–electrical single-spin read-out was recently established, and a long nuclear spin coherence time demonstrated for an ensemble of P ions in highly purified ^{28}Si (ref. 12). The spin ensemble was read out by detecting the photocurrent generated when the 1,078-nm excitonic transition associated with the P ions was excited. In the present work, we demonstrate single-site detection by electrically detecting the optical excitation of the $^4I_{15/2}$–$^4I_{13/2}$ transition of single Er ions implanted into silicon, resolving both electronic Zeeman and hyperfine structure. The efficient read-out required for single-site detection is achieved by measuring the photo-induced change in the site's charge state using a single-electron transistor (SET), rather than by detecting the associated photocurrent.

The large magnetic moment of erbium's electronic ground state, the $I = 7/2$ nuclear spin of the ^{167}Er isotope and the coincidence between the $^4I_{15/2}$–$^4I_{13/2}$ transition and the 1.5-μm transmission window of silica optical fibres make Er centres appealing for quantum information applications[13–15]. The few existing studies in samples with a high concentration of Er have shown nuclear spin relaxation times of 0.1 s (ref. 16) and electron spin dephasing times of 100 μs (ref. 15). Single-site detection grants access to low Er densities, where we expect drastically enhanced coherence times in analogy to the recent development for P in Si[12]. The low emission rate from optically excited rare-earth ions such as Er^{3+} makes pure optical detection of single sites challenging[13,14]. Recently, however, the optical detection of a single rare-earth ion was demonstrated in a Pr-doped YAG nanocrystal[17]. The technique used involved the two-step excitation of the ion to a high-lying 5*d* electron state and detection of the resultant emission[17]. The experiment was conducted at room temperature and resulted in low detection efficiency and low frequency resolution, making state read-out infeasible.

The $^4I_{15/2}$–$^4I_{13/2}$ transition is between states within the inner 4*f* electron shell of the Er^{3+} ion, which is well shielded from the surrounding lattice by filled outer shells, resulting in narrow spectral linewidths and the potential for high-resolution frequency addressing. At liquid helium temperatures, homogeneous linewidths as narrow as 50 Hz have been observed for the transition in Er^{3+}:Y_2SiO_5 (ref. 18). Until now, there have not been any sub-inhomogeneous-linewidth studies conducted on optical transition in Er centres in silicon. The observed lifetime of emission of 2 ms from the $^4I_{13/2}$ state for Er^{3+} ions in silicon implies a minimum linewidth of 150 Hz (ref. 19).

The resonant photoionization of individual Er^{3+} ions is studied in an Er-implanted SET (Fig. 1a), which works as a charge sensor. The $^4I_{15/2}$–$^4I_{13/2}$ transition of an Er^{3+} ion has a relatively high probability, when a stimulating laser is tuned to its resonant wavelength, and the Er^{3+} ion could be further ionized owing to a two-photon process or an Auger process. The charge displacement induced by an ionization event simultaneously leads to a change in the tunnelling current of the SET. To get a high sensitivity, the SET is biased close to the degeneracy point between two charge states, that is, at the edge of one Coulomb peak (Fig. 1b). Accordingly, the transconductance is large, and a small charge displacement in the sensitive region will lead to a significant change in the tunnelling current[20,21]. The photoionization of individual Er^{3+} ions leads to a significant change in tunnelling current (Fig. 1b). The $^4I_{15/2}$–$^4I_{13/2}$ transition of each Er^{3+} ion has a specific resonant photon energy, by which individual Er^{3+} ions can be distinguished. When the laser is tuned to a non-resonant wavelength, the tunnelling current mainly stays at the background level (Fig. 1c). In contrast, when the laser is tuned to a resonant wavelength of an Er^{3+} ion, the photoionization of the Er^{3+} ion leads to a rise in the tunnelling current. The current then returns to the lower level owing to its neutralization, resulting in a two-level current–time trace (Fig. 1d), which suggests that only one single Er^{3+} ion is ionized (Methods). Figure 1e shows a photoionization spectrum of a single Er^{3+} ion. Current–time traces are recorded at a series of photon energies, and then the histogram showing the distribution of binned current in time is plotted as a function of the photon energy detuning. The colour in Fig. 1e represents the time (Σt_{bin}) during which the current stays within one bin, and a 0.02-nA bin size is used throughout the analysis.

As shown in Fig. 1a, the SET has a Si channel that passes under the gate. The SET is biased below the threshold voltage, so that the current tunnels through the corner regions of the Si channel[22]. Consequently, the charge sensor is more sensitive to the Er^{3+} ions that are closer to the corner regions in the channel, and different Er^{3+} ions have different capacitive couplings leading to different detection sensitivities. The change in current (Fig. 1b–d) accords with the loss of an electron, indicating that it is due to the ionization of the Er centre, whereas

[1]Centre of Excellence for Quantum Computation and Communication Technology, School of Physics, University of New South Wales, Sydney, New South Wales 2052, Australia. [2]Centre of Excellence for Quantum Computation and Communication Technology, RSPE, Australian National University, Canberra, Australian Capital Territory 0200, Australia. [3]Centre of Excellence for Quantum Computation and Communication Technology, School of Physics, University of Melbourne, Melbourne, Victoria 3010, Australia.

©2013 Macmillan Publishers Limited. All rights reserved

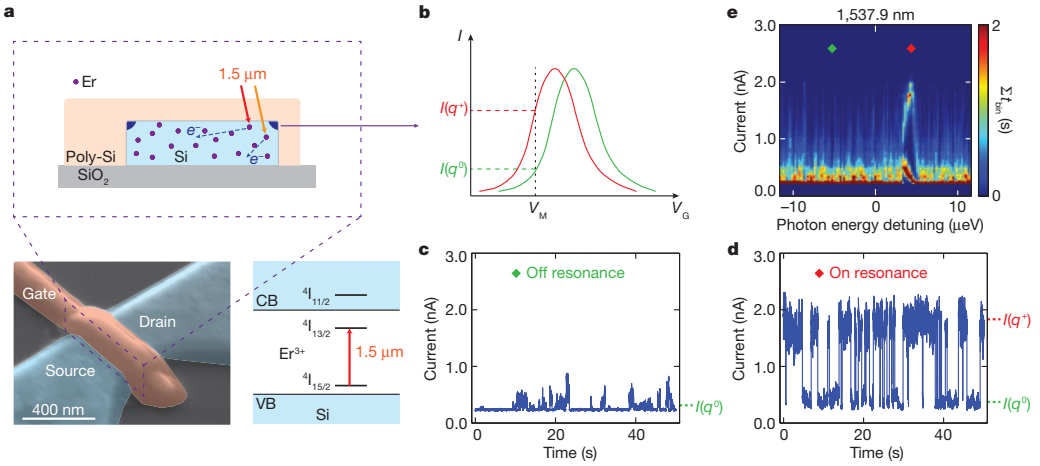

Figure 1 | Photoionization spectroscopy of an individual Er^{3+} ion. **a**, Coloured scanning electron micrograph of a typical SET device used in this study and a band structure of Er^{3+} ions in silicon. CB, conduction band; VB, valence band. Top, schematic cross-section of the SET showing the optical addressing of individual Er^{3+} ions. **b**, The SET charge-sensing scheme. The loss of an electron due to photoionization induces a transient shift of the current (I)/gate voltage (V_G) curve towards lower gate voltages, causing a change in current from $I(q^0)$ to $I(q^+)$. **c**, **d**, The current–time traces recorded for a fixed gate voltage (V_M) under non-resonant (**c**) and resonant (**d**) illumination. **e**, The histogram of current–time traces as a function of the photon energy detuning. The photon energy of the illumination is detuned with respect to the centred wavelength of 1,537.9 nm.

the gain of an electron will lead to a shift opposite to that in Fig. 1b, that is, to higher gate voltages. The small fluctuations in current, which we attribute to the trap states (defects that can capture electrons) in the gate dielectric or the oxide layer with weak capacitive coupling[23], can be suppressed by properly annealing the devices before fabrication. The read-out efficiency is mainly limited by the efficiency of the excitation from the $^4I_{13/2}$ excited state into the conduction band, which can be increased to close to 100% by increasing the intensity of the light used to drive this final ionization step. We observe resonances, using photoionization spectroscopy, mostly between 1,535 and 1,539 nm, which is consistent with the $^4I_{15/2}$–$^4I_{13/2}$ transition of Er^{3+} ions in silicon[13,14].

We next study the Zeeman effect of individual Er^{3+} ions, because the Zeeman effect is an essential tool to determine the site symmetry of Er centres. Er ions in Si tend to have a valence of 3+, characteristic of the Si lattice, and so the 4*f* electrons of Er^{3+} ions have the ground state $^4I_{15/2}$ and the first excited state $^4I_{13/2}$ (ref. 13). The degeneracy is lifted by the crystal field, such that each state splits into several levels depending on the symmetry of the Er centre[13]. The transition between the lowest level of $^4I_{15/2}$ and the lowest level of $^4I_{13/2}$ is responsible for the strong emission band around 1.54 μm, and the Zeeman splitting of those two levels in the case of double degeneracy is shown in Fig. 2a. The doublet states can be described by an effective spin of $S = 1/2$, and the Zeeman interaction has the form $H = \beta_e BgS$, where β_e is the electronic Bohr magneton, B is the magnetic field, g is the g-factor matrix[24] and S is the spin vector. The Zeeman splitting energies of the higher- and lower-energy doublets are $\Delta E_e^H = \beta_e g_H B$ and $\Delta E_e^L = \beta_e g_L B$, respectively. As shown in Fig. 2a, two types of optical transition can be excited between these doublets. The photon energy difference between two transitions of the same type can be described by $\Delta E_{photon} = \beta_e \Delta g B$, where Δg, the g-factor difference, is $|g_H + g_L|$ for $\Delta M_S = \pm 1$ transitions and $|g_H - g_L|$ for $\Delta M_S = 0$ transitions. In this study, we measured the Zeeman splitting of four spectrally isolated Er resonances, and observed g-factor differences ranging from 1.6 to 10.8.

Figure 2b, c shows the Zeeman splitting of Er^{3+} ions. Current–time traces are recorded at a series of photon energies and magnetic fields; each pixel in Fig. 2b, c represents one trace. When an Er^{3+} ion is ionized, the current will exceed a certain threshold, which is determined by the background current fluctuation under non-resonant illumination. For each current–time trace, the time (t_{up}) during which the current exceeds the threshold is integrated and gives the values (Σt_{up}) plotted in Fig. 2b, c. As shown in Fig. 2b, the resonance occurs at a photon energy detuning of 1 μeV away from 1,535.8 nm at zero magnetic field, and starts to split into two diagonal arms as the magnetic field increases. It is due to the Zeeman effect of one individual Er^{3+} ion, with $\Delta g \approx 4.8$. Similarly, the Zeeman splitting of the resonance around 1,538.0 nm is studied as shown in Fig. 2c, where the darkest blue rectangular regions were not scanned. There seem to be two resonances with similar resonant wavelengths and the same g-factor difference ($\Delta g \approx 3.3$), but with different signal intensities. This could be due to two individual Er^{3+} ions with the same site symmetry but with different capacitive couplings. Furthermore, the Zeeman splitting of the resonance around 1,538.0 nm shows polarization dependence. As shown in

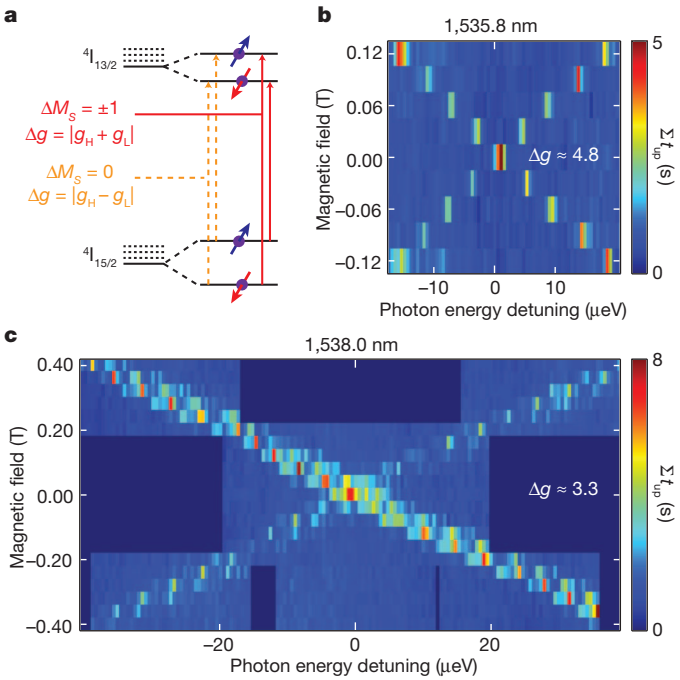

Figure 2 | The Zeeman effect of individual Er^{3+} ions. **a**, Schematic diagrams showing the Zeeman splitting and optical transitions of Er^{3+} ions in silicon. The splitting of the $^4I_{13/2}$ and $^4I_{15/2}$ states depends on the site symmetry of the Er centre. **b**, The Zeeman splitting scan of the Er resonance with a centred wavelength of 1,535.8 nm. Each pixel represents a current–time trace recorded for 50 s. **c**, The Zeeman splitting scan of the Er resonance with a centred wavelength of 1,538.0 nm.

©2013 Macmillan Publishers Limited. All rights reserved

Fig. 2c, the diagonal arm is weaker than the anti-diagonal one. By modifying the polarization of the light entering the cryostat, we tuned the diagonal arm to be stronger than the anti-diagonal one. The site symmetry of individual Er centres can be determined from the polarization dependence and a rotating magnetic field measurement. Spin-selective excitation even for degenerate spin states can be achieved by maximizing the contrast between two Zeeman arms (Fig. 2c), which allows spin read-out without a magnetic field.

The hyperfine structure is of great interest because the nuclear spin has long coherence times useful for quantum information storage[12,25,26]. In addition, this structure is an effective means of distinguishing between different ions as well as other defects. Erbium has six stable isotopes, among which only ^{167}Er has a non-zero nuclear spin, of $I = 7/2$, leading to eight nuclear spin states. At high magnetic field, the hyperfine interaction can be treated as a perturbation of the Zeeman effect[27], and so each electron spin state will split into eight sublevels owing to the hyperfine interaction (Fig. 3a). We denote the total splitting energies of these eight sublevels of $^4I_{15/2}$ and $^4I_{13/2}$ as ΔE_N^L and ΔE_N^H, respectively. At low magnetic field, the hyperfine interaction is comparable to the Zeeman effect, so the sublevels will mix[28].

To investigate the hyperfine structure of $^{167}Er^{3+}$ ions, we implanted ^{167}Er ions and ^{168}Er (with zero nuclear spin) control ions. We first study the photoionization spectrum of an Er^{3+} control ion with zero nuclear spin. The integrated time (Σt_{up}) is plotted as a function of the photon energy detuning, as indicated by the blue dashed line in Fig. 3b. The same spectral asymmetry as that in Fig. 1e is observed. We attribute the asymmetry to the correlation between the Stark shift of the $^4I_{15/2}$–$^4I_{13/2}$ resonance and a broadening of the Coulomb peak, both of which are sensitive to fluctuating electric fields in the channel. The fluctuating field is attributed to the laser excitation of trap states in or near the channel. Because we directly observe the effect on the Coulomb peak, it is possible to remove part of this broadening of the peak. After applying this correction (Methods), a minimum spectral full-width at half-maximum of 50 neV is observed as indicated by the red solid line in Fig. 3c. To significantly reduce the linewidth further, it will be necessary to reduce the density of trap states. As well as undergoing electric-field-induced shifts, the line is expected to be broadened through magnetic interactions with both ^{29}Si, by up to tens of nanoelectronvolts, and paramagnetic centres in the device. It is expected from analogy with observations in Er^{3+}:Y_2SiO_5 (ref. 18) that applying a large magnetic field will suppress broadening by this mechanism.

We now show the hyperfine structure of one $^{167}Er^{3+}$ ion. The photoionization spectrum recorded at high magnetic field ($B = 0.14$ T) (Fig. 3c) reveals eight resonant peaks with a photon energy difference of about 0.2 μeV between each successive pair. The high spectral resolution allows nuclear spin read-out with potential for single-shot read-out and manipulation of the nuclear spin states. Because the addressability does not rely on a specific magnetic field, the photoionization spectra are measured at a series of magnetic fields (Fig. 3d). The Zeeman shift is subtracted to show the evolution of the hyperfine interaction. At high magnetic field, eight significant peaks are observed in total (for $0.08\ \mathrm{T} \leq B \leq 0.14\ \mathrm{T}$), because here the hyperfine interaction can be treated as a perturbation of the Zeeman effect. At low magnetic field, multiple resonances appear (for $-0.04\ \mathrm{T} \leq B \leq 0.06\ \mathrm{T}$), revealing the mixing of the hyperfine sublevels, because here the hyperfine interaction is comparable to the Zeeman effect.

The eight significant peaks, representing the eight different nuclear spin states of ^{167}Er, demonstrate that the resonances are due to the $^{167}Er^{3+}$ ion rather than to other ions or defects. The peaks (Fig. 3c) correspond to the allowed transitions ($\Delta M_I = 0$) preserving the nuclear spin states, but the question remains of whether they are due to the $\Delta M_S = 0$ transitions or the $\Delta M_S = \pm 1$ transitions. As shown in Fig. 3a, we attribute them to the $\Delta M_S = 0$ transitions for two reasons. First, the energy difference between the two most distant hyperfine peaks is only about 1.7 μeV (Fig. 3c), which is much smaller than the typical splitting energy of the $\Delta M_S = \pm 1$ transitions of Er^{3+} ions. Electron paramagnetic resonance measurements on $^{167}Er^{3+}$ ions in crystals show a splitting energy ($2\Delta E_N^L$) of about 30 μeV (refs 15, 29), which corresponds to the $\Delta M_S = \pm 1$ transitions. Second, a ninth peak appears beyond the region between the two most distant peaks (at a photon energy detuning of −1.1 μeV in Fig. 3c). This peak is recognizable but is much weaker than the other eight peaks, a weakness that we attribute to a forbidden transition. The energy of the forbidden transitions ($\Delta M_I = \pm 1$) of Er^{3+} ions can lie outside the region between the two most distant peaks of the allowed transitions, but only in the case of the $\Delta M_S = 0$ transitions. Consequently, the eight significant peaks are attributed to the $\Delta M_S = 0$ transitions, and the splitting energy is expressed as $|\Delta E_N^H - \Delta E_N^L| = 1.7$ μeV.

Hybrid optical–electrical access to single spins of individual ions in a nanotransistor has been demonstrated, and is applicable to other defects in solids. Specifically, with an Er-implanted SET, photoionization spectroscopy allows real-time observation of single optical excitation events, avoiding the bottleneck of photon collection. Furthermore, high-resolution optical frequency addressing circumvents the limitations due to thermal broadening in earlier electrical detection of impurity spins[1]. Our findings open the way to the optical addressing and manipulation of the electron and nuclear spin states of individual defects in a solid, other than nitrogen–vacancy centres in diamond. In addition, this hybrid optical–electrical technique advances the microstructural study of ions in a semiconductor to the single-site level, including microscopic aspects, electrical and optical activity, and so on.

An approach that combines dopant ions (for example Er and P) with quantum optical control and semiconductor fabrication technologies represents an attractive platform with which to realize a scalable quantum computation and communication architecture. Such a system could consist of individual ions inside a ring cavity coupled to

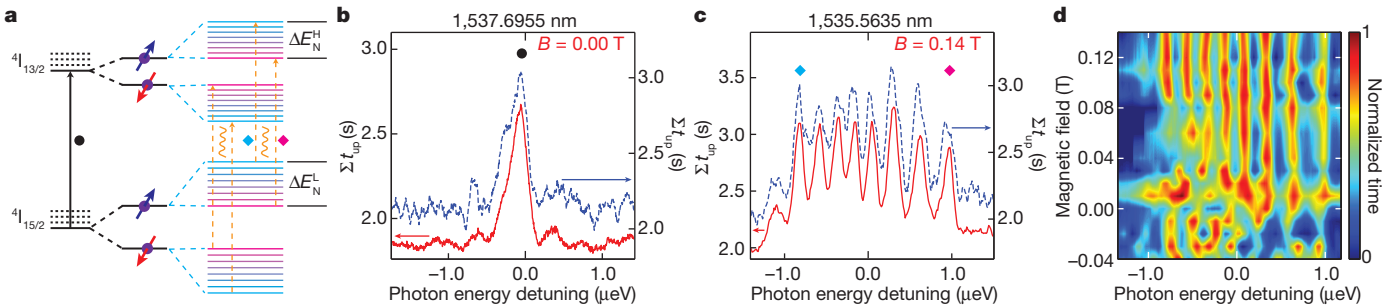

Figure 3 | The hyperfine structure of an individual Er^{3+} ion. **a**, Schematic diagrams showing the hyperfine splitting and the $\Delta M_S = 0$ transitions (orange dashed line) of $^{167}Er^{3+}$ ions at high magnetic field, and, for comparison, the optical transition of Er^{3+} ions with zero nuclear spin at zero magnetic field (black solid line). **b**, The photoionization spectrum of an Er^{3+} control ion with zero nuclear spin. The red solid and blue dashed lines respectively represent the data with and without removing the broadening. **c**, The photoionization spectrum of a single $^{167}Er^{3+}$ ion. The eight significant peaks correspond to optical transitions of the eight nuclear spin states of ^{167}Er ($I = 7/2$). **d**, The contour plot of the photoionization spectra of the $^{167}Er^{3+}$ ion, showing evolution of the hyperfine interaction.

©2013 Macmillan Publishers Limited. All rights reserved

each other via photons, with nearby charge-sensing devices used to read out the spin states of individual ions and to control the coupling between ions by Stark tuning. The ring cavities could be connected by optical waveguides, which enable quantum information transfer between individual ions in different cavities. Here we have demonstrated the first step towards such a system, that is, optical addressing of individual ions, and further improvement can be made by reducing the observed linewidth as discussed above. However, there are essential issues to be addressed in the future, such as electron and nuclear spin coherence times of Er and P ions, the influence of photoionization on nuclear spin coherence and spin–photon entanglement.

Note added in proof: During the production of the manuscript we became aware of new all-optical single-spin detection of defect centres (ref. 31 and F. Jelezko, personal communication), which further illustrates the attractiveness of a hybrid electrical–optical approach.

METHODS SUMMARY

The devices were fabricated at IMEC as previously described[30]. After complete device fabrication, an Er:O co-implantation (dose ratio, 1:6) was performed with implantation energies of 400 keV (Er) and 55 keV (O). There should be approximately 30–40 Er ions in the sensitive region of one Coulomb peak. Under the erbium implantation conditions we used, the beam is estimated to have been composed of 70–80% ^{168}Er and 20–30% ^{167}Er. The devices were then annealed at 700 °C in N_2 for 10 min to remove implantation damage and to initiate the formation of Er centres. All the measurements were carried out in a liquid helium cryostat at 4.2 K. The laser beam, with an optical power of 4–5 mW, passed through a single-mode fibre and was incident on the sample with a beam diameter of about 1 mm. In the initial phase of the experiments (Figs 1 and 2), a commercial tunable laser with an external cavity was used. To maintain a high precision, we set one centred wavelength using a motor-actuator and swept the wavelength about the centred wavelength using a piezo-actuator. In the high-resolution experiments (Fig. 3), the wavelength of another laser was stabilized to about 0.01 pm, and a wavelength meter was used to compensate the thermal drift.

Full Methods and any associated references are available in the online version of the paper.

Received 12 December 2012; accepted 18 March 2013.

1. Morello, A. *et al.* Single-shot readout of an electron spin in silicon. *Nature* **467,** 687–691 (2010).
2. Fuechsle, M. *et al.* A single-atom transistor. *Nature Nanotechnol.* **7,** 242–246 (2012).
3. Pla, J. J. *et al.* A single-atom electron spin qubit in silicon. *Nature* **489,** 541–545 (2012).
4. Gaebel, T. *et al.* Room-temperature coherent coupling of single spins in diamond. *Nature Phys.* **2,** 408–413 (2006).
5. Jiang, L. *et al.* Repetitive readout of a single electronic spin via quantum logic with nuclear spin ancillae. *Science* **326,** 267–272 (2009).
6. Togan, E. *et al.* Quantum entanglement between an optical photon and a solid-state spin qubit. *Nature* **466,** 730–734 (2010).
7. Maze, J. R. *et al.* Nanoscale magnetic sensing with an individual electronic spin in diamond. *Nature* **455,** 644–647 (2008).
8. Morton, J. J. L., McCamey, D. R., Eriksson, M. A. & Lyon, S. A. Embracing the quantum limit in silicon computing. *Nature* **479,** 345–353 (2011).
9. Zwanenburg, F. A. *et al.* Silicon quantum electronics. Preprint at http://arxiv.org/abs/1206.5202 (2012).
10. Robledo, L. *et al.* High-fidelity projective read-out of a solid-state spin quantum register. *Nature* **477,** 574–578 (2011).
11. Neumann, P. *et al.* Single-shot readout of a single nuclear spin. *Science* **329,** 542–544 (2010).
12. Steger, M. *et al.* Quantum information storage for over 180 s using donor spins in a ^{28}Si "semiconductor vacuum". *Science* **336,** 1280–1283 (2012).
13. Kenyon, A. J. Erbium in silicon. *Semicond. Sci. Technol.* **20,** R65 (2005).
14. Vinh, N. Q., Ha, N. N. & Gregorkiewicz, T. Photonic properties of Er-doped crystalline silicon. *Proc. IEEE* **97,** 1269–1283 (2009).
15. Bertaina, S. *et al.* Rare-earth solid-state qubits. *Nature Nanotechnol.* **2,** 39–42 (2007).
16. Baldit, E. *et al.* Identification of Λ-like systems in Er^{3+}:Y_2SiO_5 and observation of electromagnetically induced transparency. *Phys. Rev. B* **81,** 144303 (2010).
17. Kolesov, R. *et al.* Optical detection of a single rare-earth ion in a crystal. *Nature Commun.* **3,** 1029 (2012).
18. Sun, Y., Thiel, C. W., Cone, R. L., Equall, R. W. & Hutcheson, R. L. Recent progress in developing new rare earth materials for hole burning and coherent transient applications. *J. Lumin.* **98,** 281–287 (2002).
19. Priolo, F., Franz, G., Coffa, S. & Carnera, A. Excitation and nonradiative deexcitation processes of Er^{3+} in crystalline Si. *Phys. Rev. B* **57,** 4443 (1998).
20. Pioda, A. *et al.* Single-shot detection of electrons generated by individual photons in a tunable lateral quantum dot. *Phys. Rev. Lett.* **106,** 146804 (2011).
21. Hanson, R., Petta, J. R., Tarucha, S. & Vandersypen, L. M. K. Spins in few-electron quantum dots. *Rev. Mod. Phys.* **79,** 1217–1265 (2007).
22. Sellier, H. *et al.* Subthreshold channels at the edges of nanoscale triple-gate silicon transistors. *Appl. Phys. Lett.* **90,** 073502 (2007).
23. Tettamanzi, G. C. *et al.* Interface trap density metrology of state-of-the-art undoped Si n-FinFETs. *IEEE Electron Device Lett.* **32,** 440–442 (2011).
24. Guillot-Nol, O. *et al.* Hyperfine interaction of Er^{3+} ions in Y_2SiO_5: an electron paramagnetic resonance spectroscopy study. *Phys. Rev. B* **74,** 214409 (2006).
25. Hedges, M. P., Longdell, J. J., Li, Y. & Sellars, M. J. Efficient quantum memory for light. *Nature* **465,** 1052–1056 (2010).
26. Simmons, S. *et al.* Entanglement in a solid-state spin ensemble. *Nature* **470,** 69–72 (2011).
27. Smith, K. F. & Unsworth, P. J. The hyperfine structure of ^{167}Er and magnetic moments of ^{143,145}Nd and ^{167}Er by atomic beam triple magnetic resonance. *Proc. Phys. Soc.* **86,** 1249 (1965).
28. McAuslan, D. L., Bartholomew, J. G., Sellars, M. J. & Longdell, J. J. Reducing decoherence in optical and spin transitions in rare-earth-metal-ion–doped materials. *Phys. Rev. A* **85,** 032339 (2012).
29. Yang, S. *et al.* Electron paramagnetic resonance of Er^{3+} ions in aluminum nitride. *J. Appl. Phys.* **105,** 023714 (2009).
30. Lansbergen, G. P. *et al.* Gate-induced quantum-confinement transition of a single dopant atom in a silicon FinFET. *Nature Phys.* **4,** 656–661 (2008).
31. Sleiter, D. J. *et al.* Optical pumping of a single electron spin bound to a fluorine donor in a ZnSe nanostructure. *Nano Lett.*. **13**(1), 116–120 (2013).

Acknowledgements We thank R. Ahlefeldt, J. Bartholomew, R. Elliman, N. Manson and A. Morello for discussions. We also thank M. Hedges and T. Lucas for their help in the initial phase of the experiments. The devices were fabricated by N. Collaert and S. Biesemans. This work was financially supported by the ARC Centre of Excellence for Quantum Computation and Communication Technology (CE110001027) and the Future Fellowships (FT100100589 and FT110100919).

Author Contributions N.S. and J.C.M. designed and performed the implantation. C.Y., M.J.S. and S.R. designed and conducted the experiments. C.Y., M.R. and G.G.d.B. carried out the experiments. All the authors contributed to analysing the results and writing the paper.

Author Information Reprints and permissions information is available at www.nature.com/reprints. The authors declare no competing financial interests. Readers are welcome to comment on the online version of the paper. Correspondence and requests for materials should be addressed to S.R. (s.rogge@unsw.edu.au).

©2013 Macmillan Publishers Limited. All rights reserved

METHODS

Details of the devices. The devices used in this study are n-p-n field-effect transistors fabricated at IMEC as previously described[30]. Each device has a p-type silicon channel passing under a polycrystalline silicon gate separated by a gate dielectric. The p-type channel has a boron doping of $10^{18}\,cm^{-3}$. After complete device fabrication, an Er:O co-implantation is performed with respective implantation energies of 400 and 55 keV and ion fluences of 4×10^{12} and $3\times10^{13}\,cm^{-2}$. This leads to an Er:O dose ratio of about 1:6 in the channel region. Under the erbium implantation conditions we use, the beam is estimated to have been composed of 70–80% ^{168}Er and 20–30% ^{167}Er. The presence of both oxygen impurities[13] and boron impurities[32] is known to enhance the luminescence of the Er^{3+} ions in silicon. The 700 °C post-implantation anneal is within the thermal processing window for Er centre activation in silicon[32].

In the experiments, the device is biased below the threshold voltage, and only the corner regions of the silicon channel go into inversion[22]. A peak of the I–V_G curve is due to the Coulomb blockade in one of the two corner regions, where the current flows. The sensitive region is defined as the region in which one elementary charge change can be detected, taking the current noise and the transconductance of the Coulomb peak into account. The sensitive region of one Coulomb peak is estimated to be the corresponding channel-corner region, which, for the device shown in Fig. 1a, has dimensions of 100 nm × 50 nm × 20 nm (length × width × height). Simulations of the ion implantation based on SRIM[33] show that there should be approximately 30–40 Er ions in the sensitive region of one Coulomb peak.

Experimental details and data analysis. All the measurements are carried out in a liquid helium cryostat at 4.2 K. The laser beam, with an optical power of 4–5 mW, passes through a single-mode fibre and is incident on the sample with a beam diameter of about 1 mm. In the initial phase of the experiments (Figs 1 and 2), a commercial tunable laser with an external cavity is used. To maintain a high precision, we set one centred wavelength using a motor-actuator, and sweep the wavelength about the centred wavelength using a piezo-actuator. The current–time traces in Fig. 1c and Fig. 1d are recorded at two different photon energies and are consistent with the photoionization spectrum as indicated by the green and red diamonds in Fig. 1e, respectively. For instance, the current mainly stays at the background level (0.4 nA) at a photon energy detuning of −5 μeV, but jumps between two levels (1.8 and 0.4 nA) at a photon energy detuning of 4 μeV. It is worth noting that the two-level trace (Fig. 1d) suggests that only a single Er^{3+} ion is ionized. Multiple ions with different capacitive couplings will lead to current–time traces with more than two levels, and two ions with the same capacitive coupling will lead to a current–time trace with three levels once they are simultaneously ionized. We attribute the charge displacement to the ionization of an Er^{3+} ion rather than the charge fluctuations of the trap states, because all the Er^{3+} ions that we observe contribute to a shift of the Coulomb peak towards lower gate voltages. In the high-resolution experiments (Fig. 3), the wavelength of another laser is stabilized to about 0.01 pm, and a wavelength meter is used to compensate the thermal drift. The asymmetry as well as part of the broadening of the resonant peak is removed by adding an photon energy offset to the data. We then integrate the time during which the current exceeds the threshold to obtain the values plotted as the red solid line in Fig. 3b, c. For comparison, with the broadening removed the red solid line shows smaller widths and less noise than does the blue dashed line without the broadening removed. Nevertheless, the resonances in the latter are still clearly visible (Fig. 3b, c).

32. Michel, J. *et al.* Impurity enhancement of the 1.54 μm Er^{3+} luminescence in silicon. *J. Appl. Phys.* **70,** 2672–2678 (1991).
33. Ziegler, J. F., Ziegler, M. & Biersack, J. SRIM – The stopping and range of ions in matter (2010). *Nucl. Instrum. Methods Phys. Res. B* **268,** 1818–1823 (2010).

©2013 Macmillan Publishers Limited. All rights reserved